Enhanced structural properties of In_2O_3 nanoparticles at lower calcination temperature synthesised by co-precipitation method

Kian Wei Goh[1], *Mohd Rafie Johan*[1,2], *Yew Hoong Wong*[1] ✉

[1]*Department of Mechanical Engineering, Faculty of Engineering, University of Malaya, 50603 Kuala Lumpur, Malaysia*
[2]*Nanotechnology and Catalysis Research Centre, University of Malaya, 50603 Kuala Lumpur, Malaysia*
✉ *E-mail: yhwong@um.edu.my*

Published in Micro & Nano Letters; Received on 17th July 2017; Accepted on 1st November 2017

Indium oxide nanoparticles (In_2O_3 NPs) were formed by calcining the optimised as-prepared indium hydroxide ($In(OH)_3$) NPs. The as-prepared $In(OH)_3$ NPs were synthesised at optimal pH 10 through co-precipitation method at various calcination temperatures (200, 300, 400, 500, 600°C) for 2 h. Characterisation of the samples was performed by thermogravimetric (TGA and differential thermal, DTA) analysis, high-resolution transmission electron microscope (HRTEM), X-ray diffractometer (XRD), Fourier transform infrared spectroscopy, and Raman spectroscopy. The complete conversion to In_2O_3 NPs was reached at 300°C. Besides, the crystallite size of In_2O_3 NPs calculated by William-Hall equation had the same trend with the values obtained from Scherrer equation. The HRTEM images also showed that the size of In_2O_3 NPs was within the range of 15–28 nm. Clearly, their work confirmed that the smallest In_2O_3 NPs (15 nm) with homogenous particle distribution were formed at a lower calcination temperature of 300°C.

1. Introduction: In recent years, many metal oxide nanostructures such as tungsten oxide [1], titanium oxide [2, 3], germanium oxide, [4], indium oxide (In_2O_3) [5, 6] and copper oxide [7] have been synthesised and characterised as they are promising candidates for the applications in optoelectronic and electronic devices. However, the design and controllable synthesis of metal oxide nanostructures with a desired structure in terms of size and shape is still a challenge [6]. Among them, In_2O_3 is a transparent conductive semiconductor with a large direct and indirect band gaps (E_g) of around 3.6 and 2.6 eV, respectively [7–9]. In fact, In_2O_3 is an insulator in its stoichiometric state but becomes highly conductive in non-stoichiometric state [10]. In recent years, synthesis of the In_2O_3 and indium tin oxide in its thin film and bulk form has been carried out by many researchers. This is because they have gained considerable attention as favourable materials for various applications such as solar cell, gas sensors and ultraviolet lasers [11]. Besides, In_2O_3 is highly transparent to visible light. When In_2O_3 is exposed to various gases, it can adjust its electrical conductance [12]. Hence, In_2O_3 has been investigated as chemical sensors for detecting H_2, CO, CI_2 and NO_2 [12]. Jiao *et al.* [13] showed that In_2O_3 had low sensitive against deoxidising gases but high gas sensing response to low concentration of NO_2. Meanwhile, In_2O_3 films used for H_2 gas sensor had good selectivity and sensitivity to CO [14].

It is noticeable that the particles size and morphologically control of indium-based nanomaterials depend on their synthesis route and conditions [15]. Over the past decades, In_2O_3 nanostructures have been prepared with different morphologies and sizes such as nanoparticles (NPs), nanowires, nanorods and nanobelts [8, 11]. Among these, In_2O_3 NPs have good dispersion properties, large surface area, fast electron transfer ability and exceptional biocompatibility [16]. Besides, numerous synthesis methods have been carried out for indium oxide nanoparticles (In_2O_3 NPs) including physical vapor deposition, sol–gel process, hydrothermal method, laser ablation in liquid, co-precipitation, mechanochemical reaction, solvothermal method and reverse microemulsion method [10, 12, 17, 18]. The extensive literature observation revealed that co-precipitation method has the most advantages among them because of its process simplicity [19, 20], low cost [19], lower synthesis temperature [20] and more homogeneous size of NPs [21]. During this synthesis process, the nucleation and growth of NPs can be adjusted. Thus, the size distribution and crystallite size of NPs can be controlled to produce more homogeneous samples [22].

A lot of research works have reported that metal oxide NPs such as aluminium oxide (Al_2O_3), chromium oxide (Cr_2O_3) and zinc oxide (ZnO) NPs can be obtained by dehydration of the corresponding metal hydroxide in air at high temperature. As to In_2O_3 NPs, the dehydration of as-prepared indium hydroxide ($In(OH)_3$) NPs allow the conversion into In_2O_3 NPs. In addition, the desired morphologies of In_2O_3 NPs can be formed by controlling the morphologies of the as-prepared $In(OH)_3$ NPs [6]. This is because the In_2O_3 NPs are able to inherit their morphologies during the dehydration process. Meanwhile, it was indicated in the literature that the structure properties of the In_2O_3 NPs are dependent on those of the as-prepared $In(OH)_3$ NPs [23]. The formation of In_2O_3 NPs by dehydration of as-prepared $In(OH)_3$ NPs was selected as a favourable method due to its advantages. This includes desirable morphology of as-prepared $In(OH)_3$ NPs which can be easily obtained through aqueous phase method when the original morphology of the as-prepared $In(OH)_3$ NPs is kept after calcination [9, 11].

On top of that, calcination temperature is another factor that will affect the crystallite size, phase composition, surface morphology and crystallinity of the In_2O_3 NPs [24]. Specifically, removal of water and hydroxyl (OH) groups of $In(OH)_3$ NPs will lead to change in structure properties of the In_2O_3 NPs [23]. Thus, calcination temperature must be controlled since it may cause the $In(OH)_3$ NPs to come in contact with each other and form larger particles due to the inter-diffusion process during calcination [25]. It is believed that condensation reactions of as-prepared $In(OH)_3$ NPs lead to formation of inorganic networks. These inorganic networks contain stiff and strong metal-oxo-metal (M-O-M) bridges where the particle size will be increased [25]. Chen *et al.* [26] showed that the average particle size of cerium oxide nanocrystals gradually increased from 12 to 47 nm when the calcination temperature was increased from 473 to 1273 K (200–1000°C). Recently, Selvakumar *et al.* [17] synthesised In_2O_3 NPs through hydrothermal method and calcined at 400, 500 and 600°C. It was discovered that the calcination temperature increase was accompanied by the increase in crystallite size of In_2O_3 NPs from 25 to 40 nm. However, the investigation regarding the effect of different

doi: 10.1049/mnl.2017.0540

calcination temperature on the structural properties of In_2O_3 NPs is still not fully exposed.

Furthermore, calcination time is another critical factor which may also affect the morphology and crystallinity of the NPs [27]. This can be explained by the crystal growth mechanism of In_2O_3 NPs during calcination. In fact, both nucleation and crystal growth occurred throughout the precipitates rather than the surfaces only which led to the change in structural properties of the NPs in terms of its morphology, crystallinity and crystallite size [28]. However, it was noticeable that the optimised In_2O_3 NPs were formed with calcination duration about 2 h [29]. Xiao *et al.* [27] have studied on the time-dependent calcination of In_2O_3 NPs. They showed that the formation of optimised In_2O_3 NPs with high crystallinity is reached when the calcination time was 2 h.

A variety of studies on the synthesis of In_2O_3 NPs was reported in [3, 4, 30]. There are many research works mainly focusing on the synthesis and characterisation of In_2O_3 NPs with both different types of precursors and/or synthesis methods [10, 31–33]. First and foremost, Zhang *et al.* [31] have used low-cost indium nitrate hydrate ($In(NO_3)_2{\cdot}4.5H_2O$) as a precursor to synthesise In_2O_3 NPs via sol–gel method. One of the fundamental reasons is because their structures and electrical properties were characterised. Second, Niederberger *et al.* [34] have studied on the effects of solvent and metal oxide precursor on the crystallite size of In_2O_3 NPs. Third, Souza *et al.* [33] have synthesised In_2O_3 NPs using a non-surfactant room temperature soft chemical method and studied their thermal, structural, microstructural and optical properties. In addition, Bagheri *et al.* [10] reported on the preparation method and structural properties of In_2O_3 NPs synthesised by both sol–gel and hydrothermal methods. Apart from these, it is believed that both pH and calcination temperature will also affect the structure properties of In_2O_3 NPs [8, 17]. As a matter of fact, the stability of the aqueous solution (pH value) is important to determine the solution reactions and structural transformation in aqueous phase method [23, 35–37]. In our previous work, the as-prepared $In(OH)_3$ NPs were synthesised at different pH values via co-precipitation method and their structure properties were investigated [38]. It was found that the smallest size of as-prepared $In(OH)_3$ NPs (~11 nm) with maximum stability (3.6 mV) were synthesised at pH 10 through co-precipitation method.

Herein, we reported further work on the transformation of as-prepared $In(OH)_3$ NPs to In_2O_3 NPs by calcination process at different temperature (200, 300, 400, 500 and 600°C). The $In(OH)_3$ NPs were synthesised via co-precipitation method at optimum pH = 10 and subsequent calcination process for 2 h. The surface morphology, particle size and phase transformation of In_2O_3 NPs were characterised for different calcination temperatures.

2. Experimental: Indium oxide (In_2O_3) NPs were prepared by co-precipitation method. In particular, ammonia hydroxide (NH_4OH), ethanol and indium nitrate hydrate ($In(NO_3)_2{\cdot}9H_2O$) were used as raw materials to obtain the precursor. These reagents were obtained from Friendemann Schmidt, John Kollin and Sigma-Aldrich, respectively. Firstly, $In(NO_3)_2{\cdot}9H_2O$ was dissolved in 20 ml of distilled water. Next, the solution was stirred magnetically for 30 min at room temperature. Subsequently, NH_4OH in an aqueous solution was slowly dropped into the reaction. As a result, the white precipitate was obtained. Once the pH value of translucent solution reached 10, the resultant white precipitate was washed by ethanol and dried at 80°C for 24 h. Finally, the as-prepared anhydrous white precipitates were calcined in a furnace at 200, 300, 400, 500 and 600°C for 2 h to get bright yellow samples.

The thermal decomposition behaviour of as-prepared white precipitates was determined simultaneously by DTA and TGA using a TGA/SDTA851 Ultramicro Balance (Mettler Toledo) with a heating rate of 10°C/min from room temperature to 1000°C. The crystalline composition of the sample was characterised by PANalytical Empyrean X-ray diffractometer (XRD) equipped with Cu K_α radiation ($\lambda = 0.15406$ nm) in a scan range of $2\theta = 10$–90°, with operating current of 30 mA and voltage 40 kV. Besides, TECNAI G2 F20 HRTEM with operating voltage of 200 kV was used to investigate the surface morphology of the samples. In this Letter, the Raman spectra of the samples were analysed through Horiba Xplora One Raman spectrometer. In addition, Perkin Elmer Spectrum 400 FTIR spectrometer was used to characterise the functional group of the samples in the range of 4000–400 cm^{-1}.

3. Results and discussion

3.1. Thermogravimetric (DTA) analysis: In this Letter, the as-prepared $In(OH)_3$ NPs are oxidised to In_2O_3 NPs by calcination. Before the calcination process was conducted, the thermal decomposition behaviour of the as-prepared $In(OH)_3$ NPs were investigated via TGA and DTA in the temperature range from 25 to 1000°C. Meanwhile, the transition temperature of the as-prepared $In(OH)_3$ NPs was determined. Fig. 1 shows the typical DTA and TGA curves of the as-prepared $In(OH)_3$ NPs synthesised via co-precipitation method. From the TGA curve of the as-prepared $In(OH)_3$ NPs, it was observed that an initial weight loss of about 10% took place at ~200°C. This is due to the absorbed water molecules desorption from as-prepared $In(OH)_3$ NPs [3, 17, 29]. Besides, it can be seen that there was a second weight loss of ~40% occurred over 200–300°C. The second weight loss was ascribed to the co-condensation reaction among the hydroxyl groups during dehydration of the as-prepared $In(OH)_3$ NPs which led to the In_2O_3 NPs formation. From here onwards, it was considered that the In_2O_3 NPs might start to form >300°C since most of the weight loss observed was related to the following reaction [3, 18]:

$$2In(OH)_3 \rightarrow In_2O_3 + 3H_2O \quad (1)$$

Furthermore, the weight loss occurred between 300 and 600°C was associated with the trapped surfactant molecules decomposition. In fact, these molecules were discovered to be surrounding the as-prepared $In(OH)_3$ NPs [17]. However, there was no obvious weight loss >600°C.

To determine its decomposition steps, the DTA analysis of as-prepared $In(OH)_3$ NPs was conducted using the similar temperature range of TGA analysis. From the analysis, the DTA curve of as-prepared $In(OH)_3$ NPs revealed that two broad endothermic peaks were located at around 180 and 280°C while an exothermic peak was identified at 390°C. These broad endothermic peaks at 180 and 280°C were assigned to the physical evaporation of water molecules from samples and de-bonding reaction of

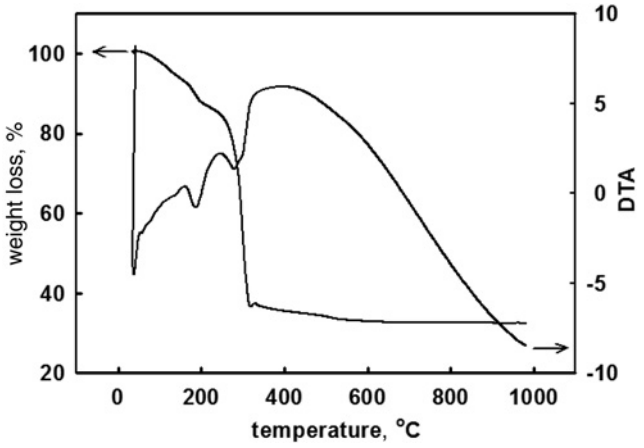

Fig. 1 *TGA and DTA curves of the as-prepared $In(OH)_3$ NPs synthesised at pH 10 via co-precipitation method*

the terminal and bridging hydroxyl groups of $In(OH)_3$ NPs, respectively [4]. The exothermic peak at 390°C was found due to the evaporation of the trapped surfactant molecules which most probably ascribed to the formation of In_2O_3 NPs [17, 30]. The DTA results complemented the results reflected in the TGA curves. Thus, it showed that the as-prepared $In(OH)_3$ NPs were decomposed completely to form In_2O_3 NPs when the temperature achieved 300°C. This phenomenon is in agreement with the results reported by Seetha and Tseng [3, 32].

3.2. X-ray diffraction (XRD) analysis: Fig. 2 shows XRD patterns of both as-prepared $In(OH)_3$ NPs and calcined In_2O_3 NPs (200, 300, 400, 500 and 600°C). Fig. 2*a* represents the XRD patterns of as-prepared $In(OH)_3$ NPs which was well-matched to the Inorganic Crystal Structure Database (ICSD) with reference code 01-076-1463 as demonstrated in our previous work [35]. In this Letter, the diffraction peaks reflected the formation of body centred cubic (bcc) phase of $In(OH)_3$ NPs synthesised at pH 10. As it was observed from Figs. 2*b–f*, the XRD patterns of calcined In_2O_3 NPs were strictly matched to the ICSD with reference code 01-071-2194. The peaks of calcined In_2O_3 NPs were present at angles of $2\theta = 30.88°$, 35.71°, 51.30°, 60.76°, 83.37° and 85.84° which correspond to the (222), (cao0), (440), (622), (662) and (048) planes, respectively. All diffraction peaks of calcined In_2O_3 NPs were ascribed to the cubic structure with lattice constant, $a = 10.1170$ Å. Therefore, it was indicated that original morphology of the $In(OH)_3$ NPs is kept after calcination. Moreover, the peak intensity of In_2O_3 NPs increased when the calcination temperature was increased from 200 to 600°C. This can be explained by improved crystallinity of In_2O_3 NPs formed at higher temperatures [17]. Additionally, the short-range order of the samples has an inherent tendency to become a long-range order which will increase the intensity of XRD pattern [17, 36]. Besides, it is noticed that a few diffraction peaks of cubic $In(OH)_3$ were detected at 200°C. The presence of $In(OH)_3$ peaks indicated that transformation of cubic $In(OH)_3$ NPs to In_2O_3 NPs was not finished. However, $In(OH)_3$ NPs peaks disappeared when the calcination temperature was increased to 300°C. Hence, these results indicate that the conversion of $In(OH)_3$ NPs to In_2O_3 NPs depends on the calcination temperature [17].

The crystallite size of the In_2O_3 NPs was estimated using the Debye-Scherrer formula [37, 38]:

$$D = \frac{K\lambda}{\beta_D \cos\theta} \tag{2}$$

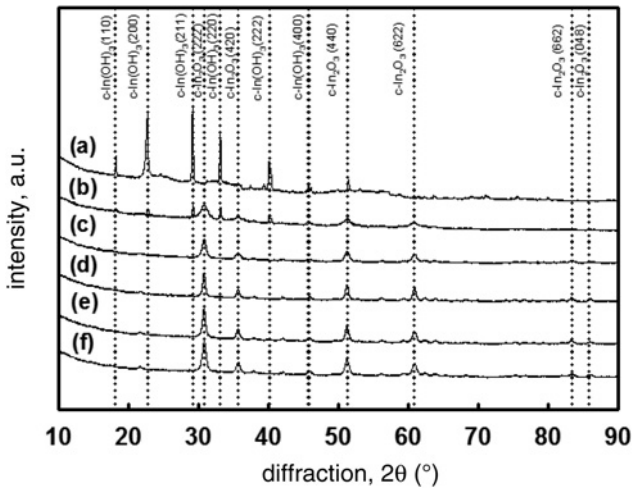

Fig. 2 *XRD patterns of $In(OH)_3$ NPs and In_2O_3 NPs*
a As-prepared $In(OH)_3$ NPs
b–f In_2O_3 NPs calcined at 200, 300, 400, 500 and 600°C, respectively

where K is the Scherrer constant (0.9), β_D is the full width at half maximum of diffraction peak, λ is the radiation wavelength, and θ is the peak position. The average crystallite size of In_2O_3 NPs was determined by all of the presented diffraction peaks. Moreover, Fig. 3 shows the average crystallite size of In_2O_3 NPs for different calcination temperature of 200, 300, 400, 500 and 600°C which are 5.16, 3.36, 3.66, 4.57 and 4.90 nm, respectively. Based on the results, a slightly decreased in the crystallite size of In_2O_3 NPs at 300°C is supposed. This is because of the shrinking of crystallite size when the as-prepared $In(OH)_3$ NPs completely transformed into In_2O_3 NPs [11]. It is well known that the as-prepared $In(OH)_3$ NPs are subjected to decomposition at high temperature which water and other volatile matter give off and In_2O_3 NPs are produced. However, in this Letter, the crystallite size of In_2O_3 NPs increased when exposed to the temperature range of 300–600°C. This can be explained through the coalescence of NPs with increasing calcination temperature which resulted in the formation of larger crystallites [17]. Similarly, this phenomenon was also reported by Seetha *et al.* [36] which involved the preparation of cubic In_2O_3 at 300, 500 and 700°C by hydrothermal method. They observed that the average crystallite size of cubic In_2O_3 gradually increased from 37 to 40 and 43 nm. In addition, Forsh *et al.* [39] also showed that the size of In_2O_3 NPs synthesised by sol–gel method increased from 8 to 20 nm when the calcination temperature was increased.

Furthermore, the crystallite size of In_2O_3 NPs was estimated from Williamson–Hall (W–H) models as [40]

$$\beta_{hkl}\cos\theta = \frac{K\lambda}{D} + 4\varepsilon\sin\theta \tag{3}$$

Fig. 4 shows the W–H plot analysis for all the samples. $K\lambda/D$ is the intercept of the graph where D can be calculated from the values and ε (strain) is the gradient of the graph. Besides, five points with goodness of fit (r^2) of 0.9377 – 0.9962 were selected from the distribution values. The relationships of crystallite size, strain and calcination temperature are shown in Fig. 5 where the crystallite size of In_2O_3 NPs decreased from 27.79 to 16.03 nm when the calcination temperature increased from 200 to 300°C. On the contrary, the crystallite size of In_2O_3 NPs increased slightly from 19.58, 22.66 to 27.19 nm when the calcination temperature was continually increased from 400, 500 to 600°C, respectively. Furthermore, the microstrains of In_2O_3 NPs for different calcination temperatures (200, 300, 400, 500 and 600°C) were 0.0736, 0.0944, 0.1144, 0.1500 and 0.1647, respectively. Therefore, a similar trend was identified in the crystallite size of In_2O_3 NPs after analysing the

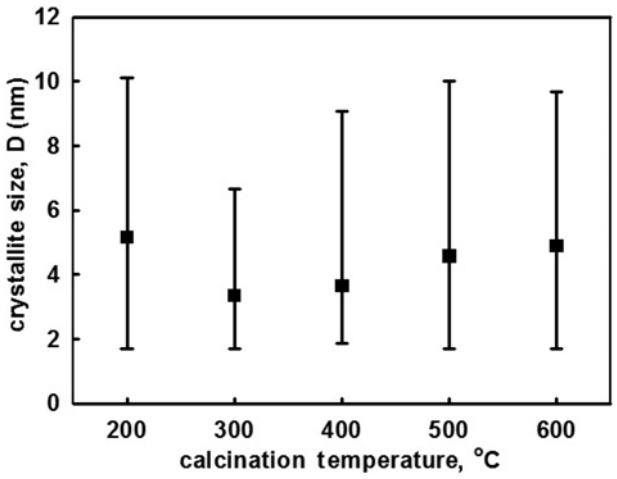

Fig. 3 *Crystallite size of In_2O_3 NPs calcined at different temperatures (200, 300, 400, 500 and 600°C)*

doi: 10.1049/mnl.2017.0540

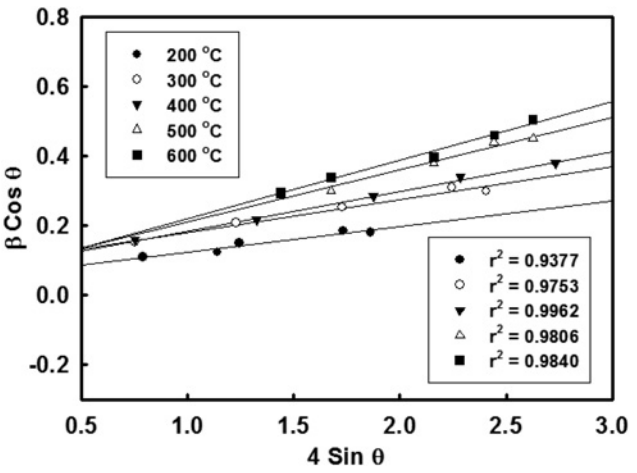

Fig. 4 *W–H plot of In_2O_3 NPs calcined at different calcination temperatures of 200, 300, 400, 500 and 600°C*

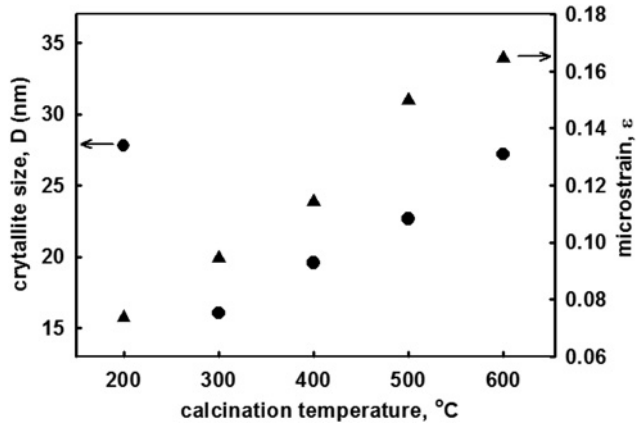

Fig. 5 *Relationship of crystallite size and microstrain of In_2O_3 NPs as the function of calcination temperatures (200, 300, 400, 500 and 600°C)*

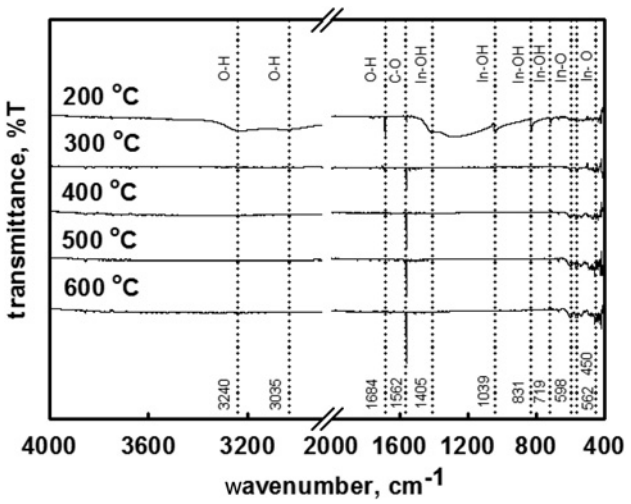

Fig. 6 *FTIR spectra of In_2O_3 NPs calcined at different temperatures (200, 300, 400, 500 and 600°C)*

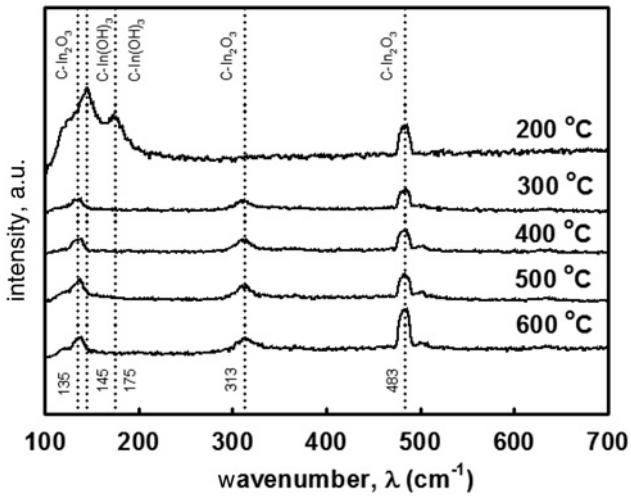

Fig. 7 *Raman spectra of In_2O_3 NPs calcined at different calcination temperatures of 200, 300, 400, 500 and 600°C*

results of both Scherrer and W–H equation. With respect to this Letter, it can be agreed that the temperature of 300°C applied to In_2O_3 NPs gives the smallest crystallite size for both calculations.

3.3. FTIR spectroscopy analysis: Fig. 6 shows the FTIR spectra (500–4000 cm^{-1}) of In_2O_3 NPs recorded for different calcination temperatures. In these spectra, the adsorption bands observed at 3240, 3035 and 1684 cm^{-1} were characteristics of bending vibrations and O–H stretching mode of hydroxyl (–OH) group which represents the presence of water molecules in the lattice [16]. The adsorption peak observed at 1562 cm^{-1} mode was assigned as the C–O stretching vibration mode which indicates the presence of ethanol. In particular, the appearance of C–O band was due to the association of the ethanol unit with indium ions (In^{3+}) to produce a longer chain and facilitate self-assembly to become an orderly shape through van der Waals interactions. Other peaks located at 1405, 1039, 831 and 719 cm^{-1} corresponded accordingly to the In–OH bonds of $In(OH)_3$ ascribed to the liberation mode of vibrations and in-plane deformation of hydroxyl groups [3, 17, 41]. Additionally, the detected peaks at 598, 562 and 450 cm^{-1} can be assigned to In–O phonon vibrations of In–OH which are the characteristic of cubic In_2O_3 [17].

It is observed that the peaks at 1562 cm^{-1} became sharper when the calcination temperatures increased from 200 to 600°C. Besides, peaks located at 3240, 3035, 1684, 1405, 1039, 831 and 719 cm^{-1} did not exhibit any infrared features of the hydroxyl groups upon further calcination at 300°C and beyond. This reveals the water loss from the samples during calcination. It can be observed that the absorption peaks of In_2O_3 at 562, 598 and 450 cm^{-1} became more intense and distinct which reflects the complete conversion of $In(OH)_3$ to In_2O_3.

3.4. Raman spectroscopy analysis: Fig. 7 shows the Raman spectra of In_2O_3 NPs recorded over the 100–700 cm^{-1} region for the temperature range from 200 to 600°C. The observed Raman shift peaks at 135, 313 and 483 cm^{-1} were ascribed to typical phonon vibrational modes of bcc-structure of In_2O_3. The Raman shift values found in this Letter well match with the values reported in [11, 36]. The first peak at 135 cm^{-1} was attributed to the In–O vibration mode of InO_6 structure units. Meanwhile, the second peak at 313 cm^{-1} corresponded to the bending vibration of $\delta(InO_6)$ octahedrons. Finally, the third peak at 483 cm^{-1} was ascribed to the stretching vibrations of the same $\nu(InO_6)$ octahedrons.

In addition, the bcc-structure of $In(OH)_3$ spectrum at 145 and 175 cm^{-1} was observed at 200°C [7]. With respect to this observation, it was revealed that the bcc-In_2O_3 was not formed completely

until the temperature reached 200°C. On the contrary, the bands disappeared at temperature of 300°C and above, as displayed in Fig. 7. Furthermore, the Raman results show that the intensity peaks of bcc-In_2O_3 increased slightly when the temperature was increased from 300 to 600°C. These observations verify the crystallinity improvement of bcc-In_2O_3 NPs [23, 25]. In this Letter, the results indicated that higher calcination temperatures enhance the crystallite growth of In_2O_3 NPs [26].

3.5. HRTEM analysis: Figs. 8*a*–*j* show the HRTEM images of the In_2O_3 NPs calcined at 200, 300, 400, 500 and 600°C. As derived from HRTEM analysis, In_2O_3 powder consists of NPs round cubic in shape. The dark area shows the attraction of the small particles where the larger particles are formed. Besides, the average sizes of In_2O_3 NPs under different calcination temperature of 200, 300, 400, 500 and 600°C were 18.67, 14.67, 17.67, 20.33 and 27.67 nm, respectively. It was discovered that the particle size of In_2O_3 NPs decreased when the calcination temperature was increased from 200 to 300°C. This is due to complete conversion of $In(OH)_3$ NPs to In_2O_3 NPs which occurred at 300°C. With respect to this Letter, this result is in agreement with the thermogravimetric analysis. Generally, the

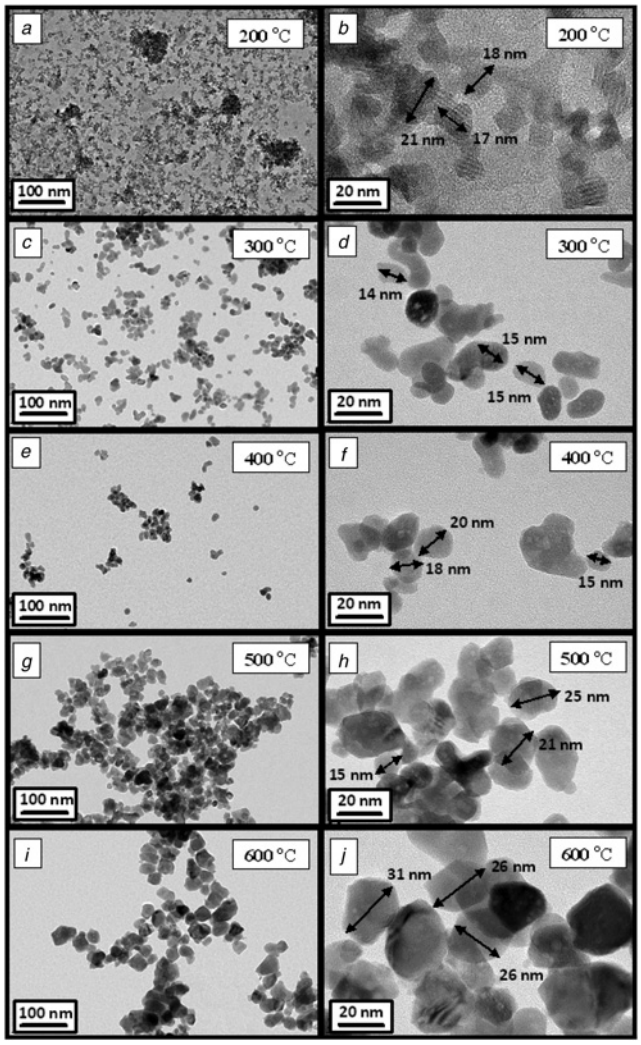

Fig. 8 *HRTEM images of In_2O_3 NPs calcined at*
a, *b* 200°C
c, *d* 300°C
e, *f* 400°C
g, *h* 500°C
i, *j* 600°C

In_2O_3 NPs size become smaller as the water molecules are evaporated from the samples. Several researchers reported that In_2O_3 NPs are usually synthesised at a higher calcination temperature >300°C via aqueous phase method [17, 27]. For instance, Selvakumar *et al.* [17] reported that the particle size of In_2O_3 NPs is about 35 nm when they were produced by calcination at 400°C through hydrothermal method. Xiao *et al.* [27] also showed that the as-prepared $In(OH)_3$ NPs were completely converted into 20 nm of In_2O_3 NPs after calcining at 500°C via solvothermal method.

On the other hand, Niederberger *et al.* [34] reported that In_2O_3 NPs of 5–15 nm were produced by mixing indium (III) acetylacetonate (precursor) with acetophenone (solvent) and calcination at 200°C for 24 h. In comparison, in our Letter, more homogeneous In_2O_3 NPs of 15 nm were produced at 300°C for shorter duration of 2 h. Besides, the particle size of In_2O_3 NPs gradually increased when the calcination temperature was increased from 300 to 600°C. The results indicated that the smaller grains tend to coalesce and form bigger particles at higher calcination temperatures, as shown in Figs. 8*d*, *f*, *h* and *j* [17].

Furthermore, the particle size distributions were observed to be more homogeneous, as presented in Figs. 8*a* and *c*. In contrast, the particle size distributions shown in Figs. 8*e*, *i* and *j* seem to be less homogeneous. In fact, both nucleation and crystal growth took place in the crystallisation of In_2O_3 NPs during calcination through the rearrangement of the In_2O_3 molecules in their amorphous phase. Both nucleation and crystal growth took place across the precipitates rather than their surfaces only. Additionally, the nucleation and crystal growth of the particles are controlled when more In_2O_3 molecules are inside the precipitates as well as the slow spread of molecules in solid state [28]. In this context, the relative smaller size of In_2O_3 NPs with higher crystallinity is expected to be produced. However, the high surface area of NPs makes them thermodynamically unstable when they may agglomerate through Van der Waals interaction [23]. Therefore, HRTEM analysis shows that the largest size of NPs (27.67 nm) with higher crystallinity were presented in this Letter when the In_2O_3 NPs was calcined at 600°C. However, in this Letter, the structure properties of In_2O_3 NPs in terms of particles size have been improved whereby the smallest size of In_2O_3 NPs (14.67 nm) were formed at a lower calcination temperature of 300°C via co-precipitation method.

4. Conclusion: To sum up, In_2O_3 NPs have been successfully prepared by calcining the as-prepared $In(OH)_3$ NPs at 200, 300, 400, 500 and 600°C. The as-prepared $In(OH)_3$ NPs are synthesised at pH 10 through co-precipitation method. The XRD pattern, FTIR and Raman spectroscopy showed that $In(OH)_3$ still rising up to 200°C in the samples. However, it is observed that pure In_2O_3 without any impurities was only present in all the samples after calcining at 300°C and beyond. Furthermore, HRTEM images also showed that the rounded cubic crystal structure of In_2O_3 NPs was formed for all of the samples. It is established that the recrystallisation of NPs occurs during calcination and the NPs tend to agglomerate at higher temperatures. The average particles size for all the samples was found to have the similar trend when the calcination temperature was increased from 200 to 600°C. These experimental results indicate that the calcination temperature is a critical factor in the formation of In_2O_3 NPs with different structure, size distribution and morphology. The crystallinity and crystallite size of In_2O_3 NPs increased with calcination temperature highlights that there is an enhancement of crystallite growth at higher calcination temperatures. This assumption is supported by FTIR, Raman and XRD analysis which displayed the peak intensity. Finally, it can be concluded that the smallest In_2O_3 NPs with well distribution were obtained at 300°C in this Letter. Therefore, the formation of In_2O_3 NPs is suggested to synthesise at optimal pH 10 and calcined at 300°C via co-precipitation method.

doi: 10.1049/mnl.2017.0540

5. Acknowledgement: This project was supported by UM/MOHE-HIR research grant (grant no. UM.C/HIR/MOHE/ENG/12) and Postgraduate Research Fund (PPP) (grant no.: PG328-2016A).

6 References

[1] Tong P.V., Hoa N.D., Duy N.V., *ET AL.*: 'Enhancement of gas-sensing characteristics of hydrothermally synthesized Wo_3 nanorods by surface decoration with Pd nanoparticles', *Sens. Actuat. B Chem.*, 2016, **223**, pp. 453–460

[2] Tshabalala P., Motaung D.E., Mhlongoa G.H., *ET AL.*: 'Facile synthesis of improved room temperature gas sensing properties of TiO_2 nanostructures: effect of acid treatment', *Sens. Actuat. B Chem.*, 2016, **224**, pp. 841–856

[3] Troitskaia I.B., Gavrilova T.A., Atuchin V.V.: 'Structure and micromorphology of titanium dioxide nanoporous microspheres formed in water solution'. Asian School-Conf. Physics and Technology of Nanostructured Materials, 2012, vol. 23, pp. 65–68

[4] Ramana C.V., Carbajal-Franco G., Vemuri R.S., *ET AL.*: 'Optical properties and thermal stability of germanium oxide (Geo_2) nanocrystals with alpha-quartz structure', *Mater. Sci. Eng. B Adv. Funct. Solid-State Mater.*, 2010, **174**, (1–3), pp. 279–284

[5] Tseng T.T., Tseng W.J.: 'Effect of polyvinylpyrrolidone on morphology and structure of In_2O_3 nanorods by hydrothermal synthesis', *Ceram. Int.*, 2009, **35**, (7), pp. 2837–2844

[6] Parast M.S.Y., Morsali A.: 'Sonochemical-assisted synthesis of nano-structured indium(III) hydroxide and oxide', *Ultrason. Sonochem.*, 2011, **18**, (1), pp. 375–381

[7] Shao F., Hernandez-Ramirez F., Prades J.D., *ET AL.*: 'Copper (Ii) oxide nanowires for P-type conductometric Nh_3 sensing', *Appl. Surf. Sci.*, 2014, **311**, pp. 177–181

[8] Zhuang Z.B., Peng Q., Liu J.F., *ET AL.*: 'Indium hydroxides, oxyhydroxides, and oxides nanocrystals series', *Inorg. Chem.*, 2007, **46**, (13), pp. 5179–5187

[9] Yang J., Frost R.L., Martens W.N.: 'Thermogravimetric analysis and hot-stage Raman spectroscopy of cubic indium hydroxide', *J. Thermal Anal. Calorim.*, 2010, **100**, (1), pp. 109–116

[10] Hu W.B., Tian D.T., Mi Y.Z., *ET AL.*: 'Synthesis and characterization of In_2O_3 nanocube via a solvothermal-calcination route', *Mater. Chem. Phys.*, 2009, **118**, (2–3), pp. 277–280

[11] Kim D.W., Kodama S., Sekiguchi H., *ET AL.*: 'Preparation of indium oxide powders by microwave plasma dehydration of indium hydroxide powders', *Adv. Powder Technol.*, 2014, **25**, (1), pp. 261–266

[12] Bagheri-Mohagheghi M.M., Shahtahmasebi N., Mozafari E., *ET AL.*: 'Effect of the synthesis route on the structural properties and shape of the indium oxide (In_2O_3) nano-particles', *Phys. E*, 2009, **41**, (10), pp. 1757–1762

[13] Guoa L.J., Shen X.P., Zhu G.X., *ET AL.*: 'Preparation and gas-sensing performance of In_2O_3 porous nanoplatelets', *Sens. Actuat. B Chem.*, 2011, **155**, (2), pp. 752–758

[14] Lin L.T., Tang L., Zhang R., *ET AL.*: 'Monodisperse In_2O_3 nanoparticles synthesized by a novel solvothermal method with in(OH)(3) as precursors', *Mater. Res. Bull.*, 2015, **64**, pp. 139–145

[15] Chung W.Y.: 'Gas-sensing properties of spin-coated indium oxide film on various substrates', *J. Mater. Sci. Mater. Electron.*, 2001, **12**, (10), pp. 591–596

[16] Tao X.J., Zhao Y.B., Sun L., *ET AL.*: 'One-pot low temperature solvothermal synthesis of In_2O_3 and InOOH nanostructures', *Mater. Chem. Phys.*, 2015, **149**, pp. 275–281

[17] Ayeshamariam A., Bououdina M., Sanjeeviraja C.: 'Optical, electrical and sensing properties of In_2O_3 nanoparticles', *Mater. Sci. Semicond. Process.*, 2013, **16**, (3), pp. 686–695

[18] Selvakumar D., Dharmaraj N., Kadirvelu K., *ET AL.*: 'Effect of sintering temperature on structural and optical properties of indium(III) oxide nanoparticles prepared with triton X-100 by hydrothermal method', *Spectrochim. Acta A Mol. Biomol. Spectrosc.*, 2014, **133**, pp. 335–339

[19] Yang H.M., Tang A.D., Zhang X.C., *ET AL.*: 'In_2O_3 nanoparticles synthesized by mechanochemical processing', *Scr. Mater.*, 2004, **50**, (4), pp. 413–415

[20] Li S.T., Qiao X.L., Chen H.G., *ET AL.*: 'Effects of temperature on indium tin oxide particles synthesized by co-precipitation', *J. Cryst. Growth*, 2006, **289**, (1), pp. 151–156

[21] Li Y., Wang J.X., Feng B., *ET AL.*: 'Synthesis and characterization of antimony-doped tin oxide (Ato) nanoparticles with high conductivity using a facile ammonia-diffusion co-precipitation method', *J. Alloys Compd.*, 2015, **634**, pp. 37–42

[22] Gupta V.K., Agarwal S., Saleh T.A.: 'Synthesis and characterization of alumina-coated carbon nanotubes and their application for lead removal', *J. Hazardous Mater.*, 2011, **185**, (1), pp. 17–23

[23] Zheng X.B., Li X.H., Huang Z.J., *ET AL.*: 'Enhanced electrochemical performance of Lini0.6co0.2mn0.2o2 cathode materials by ultrasonic-assisted co-precipitation method', *J. Alloys Compd.*, 2015, **644**, pp. 607–614

[24] Amirsalari A., Shayesteh S.F.: 'Effects of Ph and calcination temperature on structural and optical properties of alumina nanoparticles', *Superlattices Microstruct.*, 2015, **82**, pp. 507–524

[25] Tharsika T., Haseeb A.S.M.A., Akbar S.A., *ET AL.*: 'Gas sensing properties of zinc stannate (Zn_2SnO_4) nanowires prepared by carbon, assisted thermal evaporation process', *J. Alloys Compd.*, 2015, **618**, pp. 455–462

[26] Reddy C.V., Vattikuti S.V.P., Ravikumar R.V.S.S.N., *ET AL.*: 'Influence of calcination temperature on Cd0.3co0.7fe2o4 nanoparticles: structural, thermal and magnetic properties', *J. Magn. Magn. Mater.*, 2015, **394**, pp. 70–76

[27] Chen J.C., Chen W.C., Tien Y.C., *ET AL.*: 'Effect of calcination temperature on the crystallite growth of cerium oxide nano-powders prepared by the co-precipitation process', *J. Alloys Compd.*, 2010, **496**, (1–2), pp. 364–369

[28] Xiao B.X., Wang F., Zhai C.B., *ET AL.*: 'Facile synthesis of In_2O_3 nanoparticles for sensing properties at low detection temperature', *Sens. Actuat. B Chem.*, 2016, **235**, pp. 251–257

[29] Pang Y.X., Bao X.: 'Influence of temperature, ripening time and calcination on the morphology and crystallinity of hydroxyapatite nanoparticles', *J. Eur. Ceram. Soc.*, 2003, **23**, (10), pp. 1697–1704

[30] Souza C.C., Rey J.F.Q., Muccillo E.N.S.: 'Synthesis and characterization of spherical and narrow size distribution indium oxide nanoparticles', *Appl. Surf. Sci.*, 2009, **255**, (6), pp. 3779–3783

[31] Niederberger M., Garnweitner G., Buha J., *ET AL.*: 'Nonaqueous synthesis of metal oxide nanoparticles: review and indium oxide as case study for the dependence of particle morphology on precursors and solvents', *J. Sol-Gel Sci. Technol.*, 2006, **40**, (2–3), pp. 259–266

[32] Goh K.W., Johan M.R., Wong Y.H.: 'Effect of Ph variation on the stability and structural properties of in(OH)(3) nanoparticles synthesized by co-precipitation method', *Appl. Phys. A Mater. Sci. Process.*, 2016, **122**, (10), p. 907

[33] Seetha M., Meena P., Mangalaraj D., *ET AL.*: 'Synthesis of indium oxide cubic crystals by modified hydrothermal route for application in room temperature flexible ethanol sensors', *Mater. Chem. Phys.*, 2012, **133**, (1), pp. 47–54

[34] Goh K.H., Haseeb A.S.M.A., Wong Y.H.: 'Physical and electrical properties of thermal oxidized Sm_2O_3 gate oxide thin film on Si substrate: influence of oxidation durations', *Thin Solid Films*, 2016, **606**, pp. 80–86

[35] Atuchin V.V., Gavrilova T.A., Gromilov S.A., *ET AL.*: 'Low-temperature chemical synthesis and microstructure analysis of GeO_2 crystals with alpha-quartz structure', *Cryst. Growth Des.*, 2009, **9**, (4), pp. 1829–1832

[36] Lim C.S., Aleksandrovsky A., Molokeev M., *ET AL.*: 'Microwave sol-gel synthesis and upconversion photoluminescence properties of Cagd2(Wo_4)(4):Er3+/Yb3+ phosphors with incommensurately modulated structure', *J. Solid State Chem.*, 2015, **228**, pp. 160–166

[37] Lim C.S., Aleksandrovsky A.S., Molokeev M.S., *ET AL.*: 'Microwave synthesis and spectroscopic properties of ternary Scheelite-type molybdate phosphors Nasrla(Moo_4)(3):Er3+, Yb3+', *J. Alloys Compd.*, 2017, **713**, pp. 156–163

[38] Goh K.H., Haseeb A.S.M.A., Wong Y.H.: 'Effect of oxidation temperature on physical and electrical properties of Sm_2O_3 thin-film gate oxide on Si substrate', *J. Electron. Mater.*, 2016, **45**, (10), pp. 5302–5312

[39] Forsh E.A., Marikutsa A.V., Martyshov M.N., *ET AL.*: 'Charge carrier transport mechanisms in nanocrystalline indium oxide', *Thin Solid Films*, 2014, **558**, pp. 320–325

[40] Chew C.C., Goh K.H., Gorji M.S., *ET AL.*: 'Breakdown field enhancement of Si-based MOS capacitor by post-deposition annealing of the reactive sputtered ZrOxNy gate oxide', *Appl. Phys. A Mater. Sci. Process.*, 2016, **122**, (2), p. 66